

Modeling and Control of Local Electromagnetic Actuation for Robotic-Assisted Surgical Devices

Alireza Mohammadi¹, Danielius Samsonas, Florence Leong², Ying Tan², Dhan Thiruchelvam, Pietro Valdastrì, *Senior Member, IEEE*, and Denny Oetomo, *Senior Member, IEEE*

Abstract—This paper proposes an electromagnetic-based local magnetic actuation (LMA) as a novel actuation system for cases where it is required to actuate a mechanical system across a physical barrier. The main motivation for LMA is in the area of minimally invasive robotic surgery, where it is desired to actuate the surgical manipulators across the abdominal wall. In the local electromagnetic actuation approach, it is proposed that the magnetic field is produced by a pair of electromagnetic stators, acting across a physical barrier (the abdominal wall), and interacts with the magnetic field of the permanent magnet rotor on the other side of the barrier. The mathematical model of the electromechanical system is developed by exploiting the principles of synchronous motors. A control strategy was then developed to regulate the rotor speed in the presence of model uncertainties, load disturbances, and axes misalignment. Furthermore, the performance of the controllers is evaluated in two cases, with a Hall effect sensor embedded internally in the abdominal cavity close to the permanent magnet rotor and placed externally to the abdominal cavity close to the stators. The main contribution is the application of electromagnetic strategies in the unique setting of rotor actuation across a physical wall, focusing mainly on the dynamics modeling of the resulting structure and evaluation of its performance for surgical application. The proposed model and actuation strategies allow robust control of the desired speed and torque of the internal rotor, and this is demonstrated through experiments.

Index Terms—Electromagnetic coupling, medical robotics, surgery.

Manuscript received March 17, 2017; revised July 5, 2017 and August 30, 2017; accepted September 17, 2017. Date of publication October 18, 2017; date of current version December 13, 2017. Recommended by Technical Editor K. Oldham. This work was supported in part by the Royal Society. Any opinions, findings, and conclusions or recommendations expressed in this material are those of the authors and do not necessarily reflect the views of the Royal Society. (*Corresponding author: Alireza Mohammadi.*)

A. Mohammadi, D. Samsonas, F. Leong, Y. Tan, and D. Oetomo are with the Melbourne School of Engineering, University of Melbourne, Parkville, VIC 3010, Australia (e-mail: alirezam@unimelb.edu.au; dsamsonas@student.unimelb.edu.au; fleong@student.unimelb.edu.au; yingt@unimelb.edu.au; doetomo@unimelb.edu.au).

D. Thiruchelvam is with the Department of Surgery, University of Melbourne, St. Vincent's Hospital, Fitzroy, VIC 3065, Australia (e-mail: dhant@unimelb.edu.au).

P. Valdastrì is with the STORM Lab, School of Electronic and Electrical Engineering, University of Leeds, Leeds LS2 9JT, U.K. (e-mail: p.valdastrì@leeds.ac.uk).

Color versions of one or more of the figures in this paper are available online at <http://ieeexplore.ieee.org>.

Digital Object Identifier 10.1109/TMECH.2017.2764465

I. INTRODUCTION

IN THE last decade, advances in surgical technologies have focused on techniques to minimize the invasiveness of surgical procedures in order to reduce the resulting trauma on patients. Recently, minimally invasive surgery (MIS) or laparoscopic techniques are widely practiced, replacing open surgery as the preferred technique in many types of surgeries [1], [2]. Current promising approaches are developed in robotic surgery to further reduce access trauma using the laparoendoscopic single-site surgery (LESS) technique by utilizing only one incision for the entire procedures as opposed to multiple incisions in conventional MIS [3]. In all these approaches, the maneuverability of the surgical instruments is limited by the fact that these rigid-link instruments are constrained to move through the access port, which is created by a surgical incision. It results in restricted tool manipulation and limited visual feedback (restricted camera maneuverability) of the surgical environment and also the difficulty in accessing the multiple quadrants in the abdomen. To overcome these problems, it is desired to remove the rigid link connecting the external and the internal components of the surgical tools. In [4], a self-contained internal surgical instruments in the form of robotic manipulators are inserted through a small incision into the abdominal cavity and actuated through on-board dc micromotors. The approach is limited in its torque capabilities by the size of the miniaturized dc motors that can pass through the incision [5].

In the search for the ability to perform MIS with higher dexterity and sufficiently strong actuation, while maintaining (or even lowering) the level of invasiveness in the procedures, magnetic linkages were investigated recently for laparoscopic surgical devices. The use of magnetic linkages in surgical applications has been explored in various forms. A thorough review has been performed by authors [6] on the implementation of magnetic-based approaches in surgical instruments for abdominal surgeries. The approach removes the rigid mechanical link and results in surgical devices that can be completely detached from the external actuation unit and be fully inserted into the abdominal cavity. Local magnetic actuation (LMA) has been proposed as a strategy to transfer mechanical power across the abdominal wall, eliminating the need for embedded actuators and wired connections on intra-abdominal surgical devices [7]. This is done using the medium of magnetic linkage, with an external permanent magnet (PM) unit producing a magnetic field

that interacts with the internal PM rotor. The LMA technique utilizes one access incision as the entry and exit point for the internal surgical units, not as the means for rigid mechanical transmission linkages, as is the case for MIS and LESS. Additionally, with the power-generating component of the actuator placed outside the abdominal cavity, it is not constrained by the port size and intra-abdominal workspace. This leads to the possibility of incorporating larger external actuation components, capable of delivering a relevant amount of mechanical power to the surgical devices.

The implementation of the LMA concept in surgical instruments has been investigated in [8] and [21], whereby a PM-based LMA is used to retract the liver tissue. The recently developed magnetic expansion control [9] is a commercial example of LMA concept implementation used for adjusting the vertebral spine for skeletally immature patients. The results and observation from the initial investigation on the use of LMA exploiting PMs [7] highlighted the various potential technical challenges for a robust practical implementation such as variation in the abdominal wall thickness and potential of misalignment between the external and internal units. Larger magnetic distance and misalignment significantly weaken the magnetic linkage and reduce the amount of transferred torque significantly [10]. Additionally, to achieve dexterous manipulation for the surgical task within the abdominal cavity, multiple degrees of freedom (DOFs) are generally required, hence the need for multiple LMA units. The presence of multiple LMA units, with each independently regulating the motion of its rotor, produces disturbances to other units in their vicinities.

In this paper, an extension to the LMA approach in our initial study [7] is explored to improve the capability of the LMA through the use of electromagnetic coils, instead of the PMs. This idea was first introduced in [11]. In order to distinguish the proposed approach from the previous, the LMA approach proposed in this paper shall be denoted as local electromagnetic actuation (LEMA), whereby the external rotary PM unit is replaced with electromagnetic windings (see Fig. 1), acting as the external stators to the internal PM rotor. The ability to vary the actuation command to the stators in real time would allow the controller to compensate for operational uncertainties, such as load variations, variable abdominal wall thickness, and the misalignment of rotational axes of the rotors.

In this paper, the structure of the design mechanism utilizing electromagnetic windings as the external unit in Fig. 1 builds upon the concept of permanent magnet synchronous motors (PMSM): A rotating magnetic field is created by its stator windings, which results in the motion of its PM rotor. However, it has a significant difference from the PMSM in the way that the stator windings in the LEMA can only be placed extra-abdominally; hence, it is located asymmetrically to one side of the rotor [12]. This is in contrast to the structure of a PMSM, where the stator windings are arranged symmetrically around the rotor. This introduces many technical challenges in the LEMA that are not resolved in the otherwise mature technology of PMSMs. First, the circle formed by the stator arrangement of a PMSM has its center coinciding with the axis of rotation of the rotor, with a

fixed radius due to its design. In the LEMA, the variability of the location of the rotor on the other side of the barrier from the stator means that there could be lateral misalignment between the centers of that stator and the rotor, and that the distance between the stator and the rotor is a variable determined by the abdominal wall thickness. Variability in other (orientation) DOFs is also possible. Furthermore, while PMSM is well insulated from external magnetic field, the rotor of the LEMA can be readily affected by the magnetic field from another stator-rotor assembly nearby.

In terms of the controller design, the aforementioned differences between the model of PMSMs and LEMA mean that the conventional PMSM control schemes such as scalar sensorless control [17] and field-oriented control (FOC) [18] cannot be directly implemented to the LEMA, and extensions are necessary to allow the strategies to be used for the control of the LEMA system.

To successfully operate an LEMA system, different types of feedback sensors are required depending on the choice of control strategies and the set of constraints as dictated by the surgical applications. The question of whether or not to include a displacement sensor in the internal device is considered in this paper, further motivated by the fact that the internal unit is often designed to be disposable for hygiene and practicality. Alternative can be made to estimate rotor speed and position based on the back-electromotive force (back-EMF) it generates on the external stators, which is a technique that has been widely used for sensorless control of PMSMs, using sliding-mode controllers [13] or extended Kalman filters [14]. In our LEMA application, the back-EMF signal is very weak due to small PM rotor size and the relatively large distance between the rotor and the stator. Extra-abdominal placement of a Hall effect sensor is investigated in this paper, compared to the intra-abdominal placement near the PM rotor to reduce the components inserted into the abdomen.

The control strategy developed for the LEMA system needs to be robust to the variations, uncertainties, and other disturbances in the abdominal surgery applications. In this paper, we concentrate on the realization of a single-DOF LEMA (a single pair of LEMA stator and rotor), thus focusing our investigation on the following uncertainties and disturbances:

- 1) load variation at the end effector due to the load required for various surgical tasks;
- 2) variation in abdominal wall thickness from 2 cm in average build patients to 8 cm for obese patients [15] (3–5 cm is considered for this study);
- 3) possible misalignment of the rotor axis and the stator center axis upon intra-abdominal deployment and positioning for anchoring.

It should be noted that while load variation is a common problem faced by all robotic manipulators, 2) and 3) are characteristic to the LEMA.

The main contributions of this paper are as follows.

- 1) The extension of the LMA idea demonstrated in the proof-of-concept investigation in [7] and [8] to demonstrate for the first time the feasibility of actuating a PM-rotor-driven surgical manipulator located across the physical

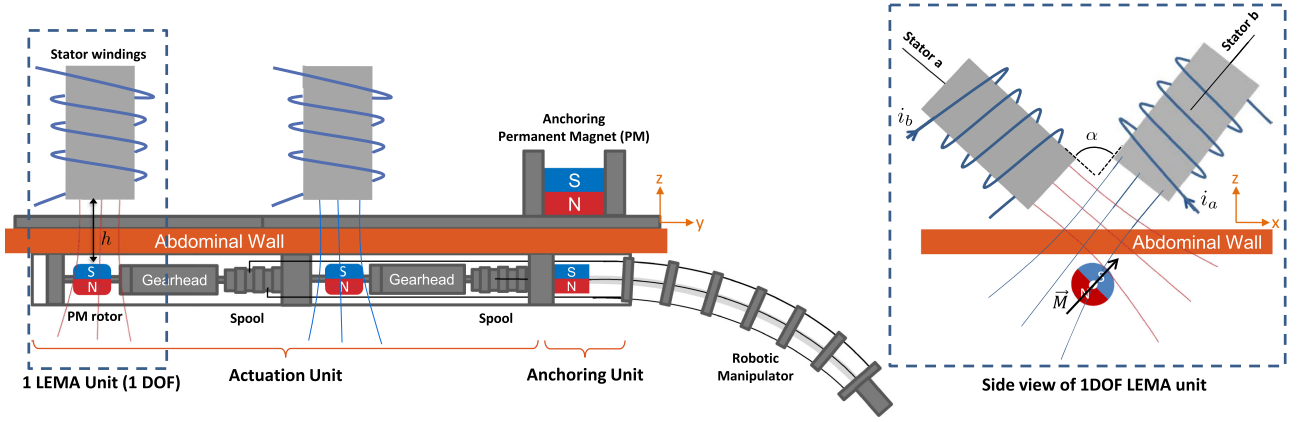


Fig. 1. Schematic of the LEMA with electromagnets as the external unit and a PM rotor as the internal unit.

- barrier through electromagnetic stator arrangement located extra-abdominally.
- 2) The development of the mathematical model of the LEMA using the electromagnetism principles and PMSM model.
 - 3) The construction of three control schemes to track the desired speed, taking into account the asymmetric structure of the LEMA physical design, model parameter variations, and load disturbances. Specifically, we investigate the open-loop sensorless scalar control (SSC) and the closed-loop FOC with internal Hall effect sensor (FOC-Int) and with external Hall effect sensors (FOC-Ext).
 - 4) The experimental validation of the LEMA concept and the evaluation of the performance of the designed controllers.

II. MATHEMATICAL MODEL OF THE LEMA

The schematic diagram of the proposed LEMA concept is depicted in Fig. 1. Two stator windings, labeled as Stator *a* and Stator *b*, are used for each rotor to produce a unique direction of the rotor motion. The stator windings are located on the outside of the abdominal wall, and a PM, acting as the rotor, is located in the abdominal cavity, immediately across the abdominal wall from the stator windings.

The motion of the rotor is the consequence of the interaction between the magnetic moment of the PM, \mathbf{M} , and the resultant magnetic field flux density of the stators, \mathbf{B} . The flux density of magnetic field produced by Stators *a* and *b* is [16]

$$B_a = \frac{Li_a}{A}, \quad B_b = \frac{Li_b}{A} \quad (1)$$

where i_a and i_b are the stator currents, L is the self-inductance of the stators, and A is the cross-sectional area of the stators. Since the magnetic field of the stators is directly proportional to the current in the stators assuming uniform magnetic field with negligible magnetic leakage, the equations can be written in terms of currents for convenience of implementation. As a result, the current of the stators is considered as a vector, which is aligned at the direction of the stator magnetic fields, as shown in Fig. 2. Therefore, the resultant magnetic field of the stators

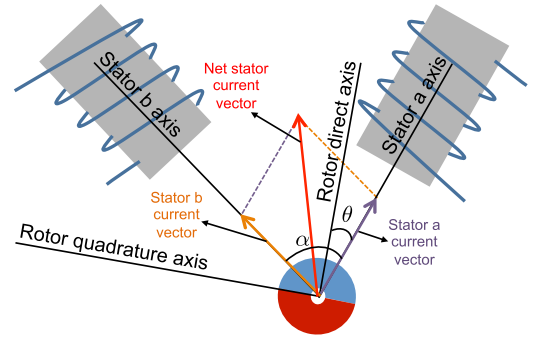


Fig. 2. Schematic diagram of the net stator current vector based on current vectors of Stator *a* and Stator *b*.

can be represented as

$$\mathbf{B} = \frac{L\mathbf{I}_s}{A} \quad (2)$$

where \mathbf{I}_s is the net stator current vector and expressed as

$$\mathbf{I}_s = i_a \hat{\mathbf{a}} + i_b \hat{\mathbf{b}} \quad (3)$$

where $\hat{\mathbf{a}}$ and $\hat{\mathbf{b}}$ are unit vectors in the direction of the stator magnetic fields. As a result, the total flux linkage resulting from stator currents is

$$\Psi_s = \mathbf{B}\mathbf{A} = L\mathbf{I}_s. \quad (4)$$

The flux linkage of each stator is the sum of flux linkage resulted from stator currents and the mutual flux linkage resulting from the PM rotor

$$\Psi_a = Li_a \hat{\mathbf{a}} + \psi_{pm} \cos(\theta) \hat{\mathbf{a}}, \quad \Psi_b = Li_b \hat{\mathbf{b}} + \psi_{pm} \cos(\theta - \alpha) \hat{\mathbf{b}} \quad (5)$$

where ψ_{pm} is the flux linkage of the rotor, α is the angle between two stators (as shown in Fig. 2), and θ is the rotor position. $\theta = 0$ is defined when the rotor direct axis is aligned in the stator *a* axis and counterclockwise is assumed positive as per convention.

The electrical system equations for the stators can be derived based on the flux variation in the windings, assuming that the resistance of the two stators is equal and the mutual inductance

between two windings is small, as follows:

$$v_a = R_s i_a + \frac{d\Psi_a}{dt}, \quad v_b = R_s i_b + \frac{d\Psi_b}{dt} \quad (6)$$

where v_a and v_b are the stator phase voltages, R_s is the resistance of the stators, and Ψ_a and Ψ_b are magnitude of Ψ_a and Ψ_b , respectively. Then, using (5), the electrical system equations are

$$v_a = R_s i_a + L \frac{di_a}{dt} + e_a, \quad v_b = R_s i_b + L \frac{di_b}{dt} + e_b \quad (7)$$

where e_a and e_b are the stators back-EMFs, which can be expressed as follows:

$$e_a = \omega \psi_{pm} \sin(\theta), \quad e_b = \omega \psi_{pm} \sin(\theta - \alpha) \quad (8)$$

where $\omega = -d\theta/dt$ is the angular speed of the rotor and clockwise rotation is positive.

The equation of motion of the rotor can be represented as

$$J \frac{d\omega}{dt} + b\omega = T_e - T_l \quad (9)$$

where J is the total moment of inertia, b is the friction coefficient, T_e is the generated electromagnetic torque, and T_l is the load torque. Damping terms from the interaction with a biological tissue is considered relatively insignificant and is neglected in this paper.

The electromagnetic torque T_e , which is produced by the interaction between the magnetic field of the PM rotor and the resultant magnetic field flux density of the stators, can be represented based on the stator currents and back-EMF voltages induced in the stators due to the rotation of PM as [19]

$$T_e = (i_a e_a + i_b e_b) / \omega \quad (10)$$

and using (8) results in

$$T_e = \psi_{pm} i_a \sin(\theta) + \psi_{pm} i_b \sin(\theta - \alpha). \quad (11)$$

This equation shows that the torque is a function of stator currents. Stator currents are, in turn, functions of PM velocity, ω [substituting (8) into (7)]. On the other hand, ω itself is a function of T_e based on (9). Therefore, these parameters are coupled and we cannot simply increase the torque by increasing the stator currents. As a result, an LEMA controller is required to provide the appropriate voltage signals to the stators such that the resulting current signals produce a smooth torque in the rotor to track a desired velocity and reject the load torque.

III. LEMA CONTROL DESIGN

A. Sensorless Scalar Control

The SSC scheme is a conventional method in PMSMs, which regulates the speed of the rotor in open loop (no feedback sensor) by varying the magnitude V , and the frequency f , of the sinusoidal voltage signals to the stator windings, where V and f are some scalar values. Increasing the frequency of the voltage signal without varying the magnitude will decrease the current supplied to the windings due to the inductance and the back-EMF terms in (7). Since the electromagnetic torque is proportional to

the current, the rotor maximum torque and consequently maximum accessible rotor speed will be decreased. This issue can be addressed by varying the frequency and the voltage simultaneously using the steady-state model of the PMSM [17]. A similar approach is employed here for the speed control of the LEMA by taking into account the phase difference between two command signals to the stators, dependent on the angle between two stators.

Based on the steady-state model of the LEMA ($di_a/dt = 0$ and $di_b/dt = 0$) and assuming that the stator resistance is negligible ($R_s = 0$), the total stator flux can be expressed using (7) as

$$V_s \cong (\psi_{pm})\omega \rightarrow \psi_{pm} \cong \frac{V_s}{2\pi f}. \quad (12)$$

Therefore, the ratio between the magnitude and frequency of the stator voltage (V_s/f) is proportional to the magnitude of the stator flux. If this ratio is kept constant, the stator flux will remain constant, and therefore, the current amplitude will be constant. As a result, the maximum torque is accessible at all speeds up to the rated rotor speed value. At any speed above the rated speed, the torque of the motor will decrease exponentially with increase of frequency, as voltage would be at its maximum [18].

This method is based on the steady-state model using magnitude and frequency of the voltage signal and ignores the dynamics involved in the variation of current (flux) in the stators. Therefore, it is not suitable for the cases where high dynamic performance is required. In addition, due to the coupling effect (both torque and flux are functions of voltage or current and frequency), the control of the current signal for constant torque is difficult [18]. FOC can address these problems by regulating the current signals in the dq frame, which rotates with the rotor.

B. Field-Oriented Control

The main goal of the FOC is to decouple the magnetizing flux (direct, d) and torque (quadrature, q) components of the stator magnetic field. In PMSMs, the stator current vectors that are equal to the number of stator pairs are projected to two stationary orthogonal axes, and then, the resultant vectors from this projection are projected to two orthogonal components in the parallel and the perpendicular directions to the axis of the rotor (dq coordinate), which is attached to the PM rotor and rotates with the same speed [19]. This projection not only decouples the stator current, but also removes the dependence on rotor angular displacement.

A conventional PMSM has at least N stator windings surrounding one rotor symmetrically in full circle, where $N \geq 3$ and the stator windings are arranged evenly $360/N$ degrees apart from each other. Therefore, current signals to subsequent stator windings are phase shifted $360/N$ degrees from each other. In the LEMA, the stator windings can only be placed on one side of the abdominal wall, and therefore, the required frame transformations should be modified accordingly.

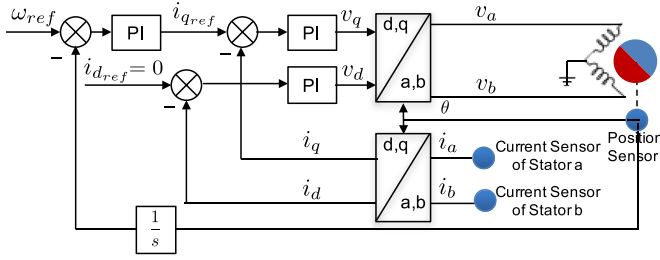


Fig. 3. Basic scheme of FOC with a PI-based controller.

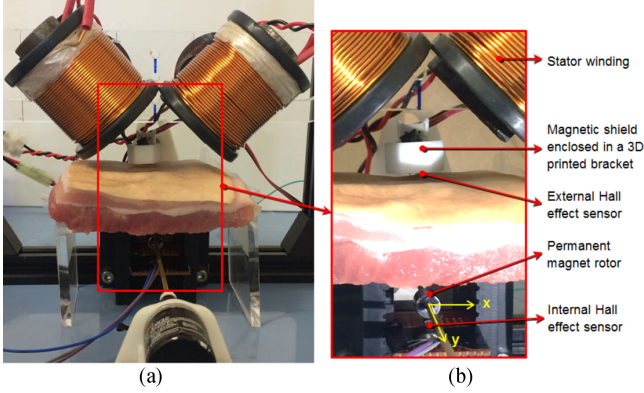


Fig. 4. Experimental setup of the LEMA and placement of Hall effect sensors. (a) Whole setup; (b) Zoom-in view.

As shown in Fig. 2, the stator currents i_a and i_b are projected to the dq coordinate, which results in

$$i_q = -\sin(\theta)i_a - \sin(\theta - \alpha)i_b \quad (13)$$

$$i_d = \cos(\theta)i_a + \cos(\theta - \alpha)i_b. \quad (14)$$

In this new coordinate system, the electrical equation (7) can be expressed as

$$v_q = R_s i_q + L_q \frac{di_q}{dt} + \omega \psi_d \quad (15)$$

$$v_d = R_s i_d + L_d \frac{di_d}{dt} - \omega \psi_q. \quad (16)$$

where $\psi_q = L_q i_q$, $\psi_d = L_d i_d + \psi_{pm}$, v_d and v_q are voltages of the stator signals, i_d and i_q are the stator currents, and L_d and L_q are the projection of stators' inductance, in the d - and q -axes, respectively. ψ_{pm} is the flux linkage due to the interaction between the PM rotor and the stators.

The electromagnetic torque in this new coordinate is

$$T_e = \psi_d i_q - \psi_q i_d. \quad (17)$$

Based on (17), in order to produce the maximum torque for a given stator current, the current on the d -axis should be set to zero. Therefore, the control goal will be simplified to producing the current signals such that the current in direct component is zero. Consequently, the produced torque is proportional to the current in the quadrature direction.

Fig. 3 shows the schematic of the implementation of a proportional–integral (PI)-based FOC for an LEMA stator and rotor unit. The required measurements are the currents in the two

stator windings and the rotor position. The measured currents, i_a and i_b , transformed into the rotor coordinate frame using (13) and (14) and its output, i_q and i_d , are compared to the reference current i_{qref} and i_{dref} , with the error driving the PI controller. The i_{qref} signal is produced by the required torque demanded by the speed regulator, and i_{dref} should be set to zero. The outputs of the current controller, v_q and v_d , are fed into the inverse coordinate transformation and then applied to the windings as v_a and v_b . It should be noted that both direct and inverse coordinate transformation requires the rotor position that can be provided by a position feedback sensor. The derivative of the position signal is also used as a rotor speed feedback signal.

IV. EXPERIMENTAL SETUP

A. Windings and Controller Hardware

The experimental setup is shown in Fig. 4. The LEMA consists of two electromagnetic windings and one PM rotor. The stator windings are identical in dimension, have 250 turns of wire, and are made of 1.32 mm of coated copper wire, which can tolerate currents up to 5 A. The cores are made of 30-mm-diameter steel rod in order to increase the electromagnetic field strength, which is proportional to the permeability of the core. The overall size of one stator winding is a cylinder with 6-cm base diameter and 6-cm height. The pair of stator coils, at 90° configuration to each other, can be contained within a volume of 8-cm height, 16-cm length, and 6-cm width. The PM is neodymium magnet (NdFeB) and has a cylindrical shape (9.5 mm in both diameter and length) with diametrical magnetization (N42 grade, 1.32 T in magnetic remanence). The diameter of the PM was selected to fit a laparoscopic device that can enter the abdominal cavity through a 12-mm surgical port. The stators are driven by two-channel 10-A Sabertooth motor driver. This driver receives a serial signal and provides pulse width modulation signal with current up to 10 A to the windings. The current in each winding is measured by a current sensor producing the analog voltage of 0–5 V proportional to the current magnitude. The hysteresis brake (Magnetic Technologies EB-3M-2DS) was attached to the shaft and used to impose controllable load torque on the rotor.

Linear Hall effect sensors (Allegro MicroSystems UGN3503UA) were used to determine the angular displacement of the PM rotor. A rotary encoder with 200 pulses per rotation (YUMO E6A2-CW3C) was attached to the shaft in order to only verify the accuracy of the Hall effect sensors. The controller is implemented using an Arduino Mega microcontroller.

B. Position and Speed Feedback Sensors

The angular displacement of the rotor is required for the direct and inverse coordinate transformation and obtaining angular velocity as feedback to the controller. To this end, two different approaches are proposed to mount the Hall effect sensors, as shown in Fig. 4(b). In the first approach, the Hall effect sensor is mounted under the PM to simulate the case where the sensor is on-board of the instrument that goes inside the body, whereas in the second approach, the Hall effect sensor is mounted in

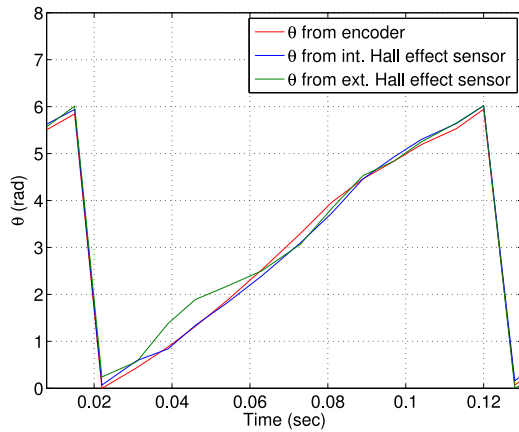


Fig. 5. Angular position measured by rotary encoder compared to estimate obtained using internal and external Hall effect sensors.

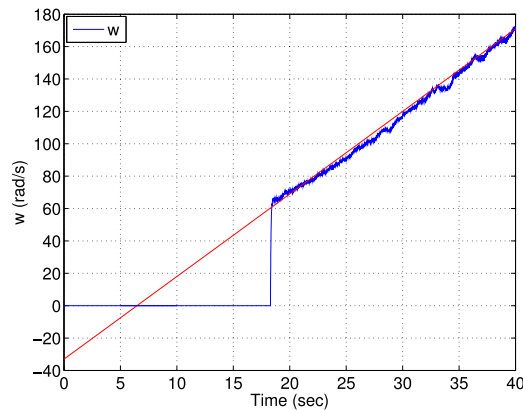


Fig. 6. Velocity response of the rotor when a torque ramp is applied.

between the windings to simulate the case where the internal instrument is sensorless, which would allow for it to be completely wireless. These approaches are explained in the following.

1) *Internal Hall Effect Sensor*: By using a single Hall effect sensor mounted close to the PM rotor, the angle θ of the shaft is equal to

$$\theta = \cos^{-1} \left(\frac{B_z}{B_{\max}} \right) \quad (18)$$

where B_z is the measured magnetic field in the z -direction and B_{\max} is the maximum magnetic field of the PM rotor. This method has proven to be very accurate when the background field is relatively small [7].

2) *External Hall Effect Sensor*: To develop a system without internal sensors, the Hall effect sensor was mounted just above the abdominal wall surface in between the windings [as shown in Fig. 4(b)]. In this case, the field measured by the sensor is a combination of fields from three sources: Stator a , Stator b , and the PM rotor. The general idea of utilizing this reading is to cancel out the effect of magnetic field of the stator windings. In order to achieve this, the current is measured in each winding, and the estimated field strengths are subtracted from the Hall effect sensor reading.

However, the PM field strength decreases as the distance from the rotor increases. Nonetheless, the distance between the windings and the sensor remains constant at all times. As a result, errors in winding's field cancellation grow relatively to the PM field strength when the abdominal wall thickness increases.

In order to minimize these errors, a makeshift magnetic shielding was used, fashioned out of an M5 nut covered with a sawn off M5 screw head, forming a dome to cover the Hall effect sensor, all enclosed in a 3-D printed casing with a cut-out directed toward the PM. In addition, a moving average low-pass filter with the window size of ten samples and sampling rate of 330 Hz is applied to the Hall effect sensor and current sensor readings to smoothen the signal before calculating the estimated field strength of the PM. The cutoff frequency (f_c) was set to be equal to the frequency of the voltage in coils, which is approximately equal to the rotation frequency of PM ($2\pi f_c \approx \omega_{PM}$).

The results of these techniques are shown in Fig. 5. This method provides angular position estimate, which is sufficiently accurate for the FOC when the distance between the PM and external Hall effect sensor is 30 mm. However, as the distance was increased to 50 mm, relative errors enlarged as expected. Although the system still worked, position errors occasionally were large enough to stall the rotor. Therefore, it was demonstrated that this method works and provides reliable performance when the distance between the PM and the external Hall effect sensor is up to 30 mm. Therefore, further improvements are necessary to make this method reliable for larger distances such as using more accurate current sensors (resolution of current sensors used in this setup is 55 mA) and Hall effect sensors and also improving magnetic shielding.

V. LEMA MODEL IDENTIFICATION AND VALIDATION

In order to design a controller for the LEMA, we need to identify the parameters in the electromechanical model. The required parameters are either measured directly or characterized through identification methods.

Stator resistance (R_s): The stator resistance is obtained from direct measurement using a digital multimeter. The measured value was $R_s = 0.8 \Omega$. It should be noted that the stator resistance is temperature dependent and the measured resistance is the value at 25 °C, but this value can change significantly due to the flow of high current through the stator. For instance, 50 °C temperature difference can cause 20% increase in the resistance value. The experiments showed the maximum operating temperature of 60 °C.

Synchronous inductances (L_q, L_d): The synchronous inductances L_q and L_d are equivalent inductances of two windings when the PM rotor is aligned with q - and d -axes, respectively. These inductances are different in general ($L_d < L_q$), although the LEMA is similar to surface-mounted PMSMs, and therefore, reluctance is the same in every position of rotor, i.e., $L_q = L_d = L$, where L is the total inductance of the stator winding. In general, the total inductance of a winding can be calculated; however, in this case, magnetic permeability of the core was unknown; therefore, the total inductance was measured using an inductance meter and was found to be $L = 5.8$ mH.

TABLE I
MODEL PARAMETERS OF THE LEMA

Resistance (R_s)	0.8 Ω
Inductance (L)	5.8 mH
Friction coefficient (b)	3.9×10^{-6} N·m·s
Total moment of inertia (J)	6×10^{-7} kg·m ²
Flux linkage of the PM rotor (ψ_{pm} @30 mm)	5×10^{-4} V·s

Inertia (J): The inertia is calculated theoretically as the shape and weight of the PM are known. The inertia of encoder and hysteresis brake were given by the manufacturer. The calculated value for the total moment of inertia is $J = 6 \times 10^{-7}$ kg·m².

Friction coefficient (b): In order obtain the viscous friction, the procedure that is proposed in [20] is employed. In this procedure, a torque ramp is applied as $T_e(t) = mt$, where t denoted the time and $m > 0$ is the ramp slope. Then, for a sufficiently long time, velocity increases in a linear fashion with the slope a . Using these data, the viscous friction can be obtained as $b = \frac{m}{a}$. Experimental results presented in Fig. 6 show velocity response of the rotor when a torque ramp of $m = 0.02$ mN·m/s was applied. The shape of the velocity response curve matched the Armstrong model presented in [20]. From the slope of the angular velocity, it was determined that $a = 5.1$; therefore, viscous friction is $b = 3.9 \times 10^{-6}$ N·m·s.

Flux linkage (ψ_{pm}): The flux linkage of the PM rotor, which is equal to its back-EMF constant, can be obtained by measuring the induced voltage between two terminals of one stator winding, while the PM is externally rotated by a dc motor. Results show that at constant speed of the dc motor, $\omega = 450$ rad/s, which is equal to the frequency of the waveform, the peak voltage V_{pk} varies with distance. Experimentally, the back-EMF constant or ψ_{pm} can be obtained as $\psi_{pm} = \frac{V_{pk}}{\omega}$. In this system, ψ_{pm} decreases over distance due to the direct proportion of the back-EMF constant to the flux density of the PM. Based on the experimental results, for abdominal wall thickness h ranging from 23 to 63 mm, back-EMF constant can be approximated as $\psi_{pm} = 11.96 \times 10^{-4} \exp(-25.97h)$ [Vs]. Based on (11), the electromagnetic torque (T_e) has a linear relation with ψ_{pm} and I_s , i.e., $T_{e_{max}} = I_s \times \psi_{pm}$. As a result, the variation in h affects ψ_{pm} and hence the resultant T_e . To verify the relation between T_e and h directly, the electromagnetic torque is measured for three different values of h at constant $I_s = 5$ A using a hysteresis brake as a dynamometer. The measured torques for $h = 23, 33, 43$ mm are $T_e = 3.1, 2.3, 1.7$ mN·m, respectively, and the calculated torques using flux linkage equation are $T_{e_{max}} = 3.3, 2.5, 2$ mN·m.

The parameters of the LEMA are summarized in Table I.

VI. EXPERIMENTAL RESULTS

In this section, the proposed control schemes in Section III are tested through experiments and will be referred as:

- 1) sensorless Scalar (V/f) Control: SSC;
- 2) FOC with an internal Hall effect sensor: FOC-Int;
- 3) FOC with an external Hall effect sensor: FOC-Ext.

These control schemes are implemented on the LEMA to track a desired speed of the PM rotor under four different situations:

- 1) no disturbance;
- 2) presence of load disturbance, T_l ;
- 3) variable wall thickness, h (see Fig. 1);
- 4) axes misalignment along, $X_{misalign}$, and perpendicular, $Y_{misalign}$, to the rotor shaft [see Fig. 4(b)].

It should be noted that, in the experimental results, start-up of the rotor rotation was delayed in some of the cases due to the calibration of the sensors at the start of the control loop. FOC-Int and FOC-Ext schemes are delayed by 1500 ms. Over this time, the internal and external Hall effect sensors were autocalibrated as the initial position of rotor was unknown at the start-up. Due to the fact that the system only has two stators, the rotor needs to be in a “manipulable” configuration for the start-up. This is done by powering only one of the two stator coils such that the PM rotor aligns to the predefined (known) angular displacement. Motion is then commenced from this angular displacement. In addition, the external Hall effect sensor was autocalibrated to adapt to the distance h .

A. Speed Control of the PM Rotor With No Disturbance

The experimental results of implementing three control approaches for the speed control of the PM rotor are shown in Fig. 7. The SSC with a predefined acceleration rate of 300 rad/s² was found to provide by far the fastest start-up of the system. The slope of the V - f profile is obtained using the model of the LEMA. The gains of PI controllers in FOC are tuned using the MATLAB PID tuning algorithm. This algorithm chooses loop bandwidth based on the LEMA dynamics model (see Table I) and designs for a target phase margin of 60°. Due to the small discrepancy between the obtained model of the LEMA and the experimental LEMA, the parameters are adjusted slightly for the best performance. The proportional (p) and integral (i) gains of the PI controller for quadrature current (q), dc (d), and rotor speed (ω) are obtained as ($K_{pq} = 0.2, K_{iq} = 1$), ($K_{pd} = 1, K_{id} = 10$), and ($K_{p\omega} = 1, K_{i\omega} = 10$), respectively. The performance of the controllers is compared in Table II with respect to the settling time (time required for the angular speed error to become less than 10% after w_r step change), overshoot (overshoot as percentage of w_r), and steady-state error (root-mean-square error (RMSE) at the steady state as percentage of w_r).

In order to show that the results are repeatable over multiple experiments, the experiments for the each of control methods was repeated for multiple runs. The plots in Fig. 7 still present the representative profile of the runs for clarity; the average value and standard deviation for the parameters of interest are summarized in Table II.

B. Robustness to Load Disturbance

The experimental results reported in this subsection aim to assess control strategies under different load torque rejection conditions. To this end, first maximum accessible torque in each

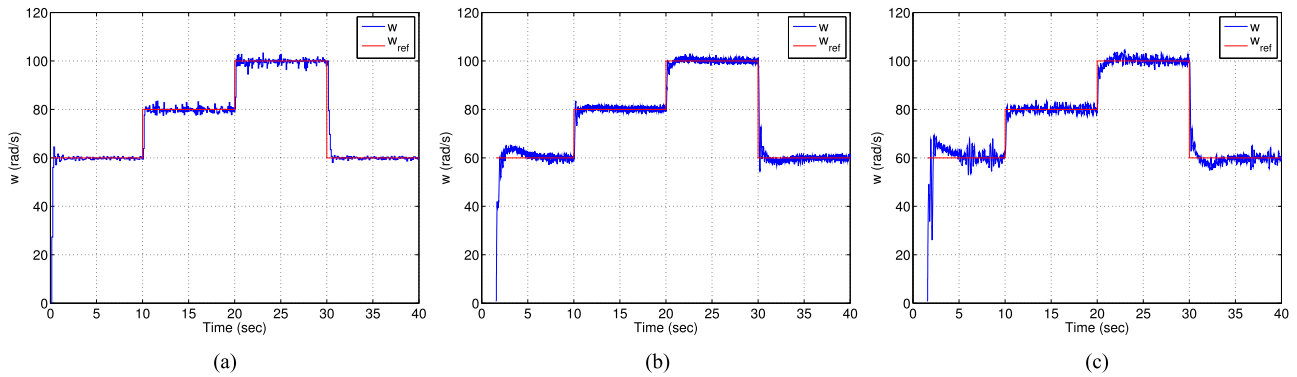


Fig. 7. Speed control of the PM rotor for $\omega_{ref} = 60, 80, 100$ rad/s at $h = 30$ mm, $T_l = 0$, $X_{misalign} = 0$, and $Y_{misalign} = 0$. (a) SSC. (b) FOC-Int. (c) FOC-Ext.

TABLE II
PERFORMANCE COMPARISON OF DESIGNED CONTROLLERS FOR SPEED TRACKING AND LOAD REJECTION AT $h = 30$ MM

	Settling time (ms)				Overshoot(%)				Std. RMSE(%)			
	0-60	60-80	80-100	100-60	0-60	60-80	80-100	100-60	60	80	100	60
w_r (rad/s)	0-60	60-80	80-100	100-60	0-60	60-80	80-100	100-60	60	80	100	60
SSC	197 ± 29	187 ± 33	164 ± 21	357 ± 42	6.2 ± 1.4	4.6 ± 0.5	2.3 ± 0.8	3.4 ± 0.7	0.6 ± 0.2	1.5 ± 0.1	1.8 ± 0.1	1.2 ± 0.8
FOC-Int	478 ± 23	143 ± 16	96 ± 13	285 ± 34	9.1 ± 2.9	5.41 ± 1.5	1.7 ± 0.7	9.4 ± 3.2	0.9 ± 0.4	0.5 ± 0.7	1.1 ± 0.2	2.5 ± 0.3
FOC-Ext	895 ± 214	108 ± 36	115 ± 26	625 ± 47	13.1 ± 5.3	2.1 ± 0.9	2.9 ± 1	6.4 ± 1.2	4.2 ± 1	0.9 ± 0.4	1.2 ± 0.3	5.3 ± 1
Load (m Nm)	0-17	17-27	27-37	37-0	0-17	17-27	27-37	37-0	17	27	37	0
SSC	0	0	0	0	1.80	2.84	2.84	3.93	1.67	1.19	1.13	1.25
FOC-Int	58	134	273	562	3.14	7.69	13.81	22.41	0.75	0.69	0.73	0.69
FOC-Ext	87	181	299	563	7.88	8.94	18.24	24.61	2.06	1.74	1.77	1.45

of the control approaches is obtained experimentally. Then, the load disturbance is applied during the speed tracking.

To investigate the maximum torque that each control scheme can transmit before rotor stalls, SSC and FOC schemes were tested under gradually increasing external load, while the reference speed, w_{ref} , was kept constant at 100 rad/s. Test results show that both SSC and FOC schemes were able to maintain angular speed of the rotor at a desired value when the current of up to 46 mA was sent to the hysteresis brake. However, when load was further increased, the rotor stalled in the case of SSC due to pole slipping, while FOC was no longer able to maintain the desired angular speed, but the rotor did not stall until the current sent to the hysteresis brake exceeded 53 mA. From the torque versus current graph of the hysteresis brake, it was found that 46 mA results in 1 - mN·m load, while 53 mA produces approximately 1.5 - mN·m load.

Once the maximum accessible torque is obtained, then the performance of the controllers is evaluated when the load disturbance is applied to the rotor. The value for T_l is adjusted by the hysteresis brake. The load rejection responses were measured while applying 0.35-, 0.7-, 0.9-, and 0-mN·m load torque [see Fig. 8(a)–(c)]. The experiments are performed at a constant 80 - rad/s reference speed. The performance of the controllers is compared in Table II.

C. Robustness to Abdominal Wall Thickness Variation

As mentioned in Section I, the average of the abdominal wall thickness upon insufflation is 20 mm. Therefore, in the previ-

ous sections, the experimental tests have been performed with 30 - mm distance between the rotor and windings. However, abdominal wall thickness can vary considerably from the average value; therefore, this section evaluates the robustness of the controllers at distance $h = 50$ mm.

Changing the distance affects the model parameters and imposes challenges to control methods. First of all, the magnetic field strength, and hence the maximum transmittable torque, decreases with distance. This limits the maximum load and acceleration of the rotor. Second, back-EMF coefficient decreases with distance and, therefore, allows us to achieve higher current at a given voltage and angular speed. However, this effect is marginal due to a very small value of back-EMF constant. Finally, as discussed in Section IV-B, position feedback is required for FOC and the error in angular position increases with distance. The experimental results are shown in Fig. 8(d)–(f) for speed tracking of 80 rad/s and load torque rejection.

D. Robustness to Axes Misalignment

In order to investigate the robustness of the controllers to axes misalignment, two cases are considered: the rotor was shifted along the rotor shaft ($X_{misalign}$) and perpendicular to the shaft ($Y_{misalign}$), as shown in Fig. 4(b). Tests were performed at a constant abdominal wall thickness of $h = 30$ mm. Experimental results are presented in Fig. 9.

Results have shown that system performance was affected only marginally by rotor misalignment of up to 20 mm in SSC

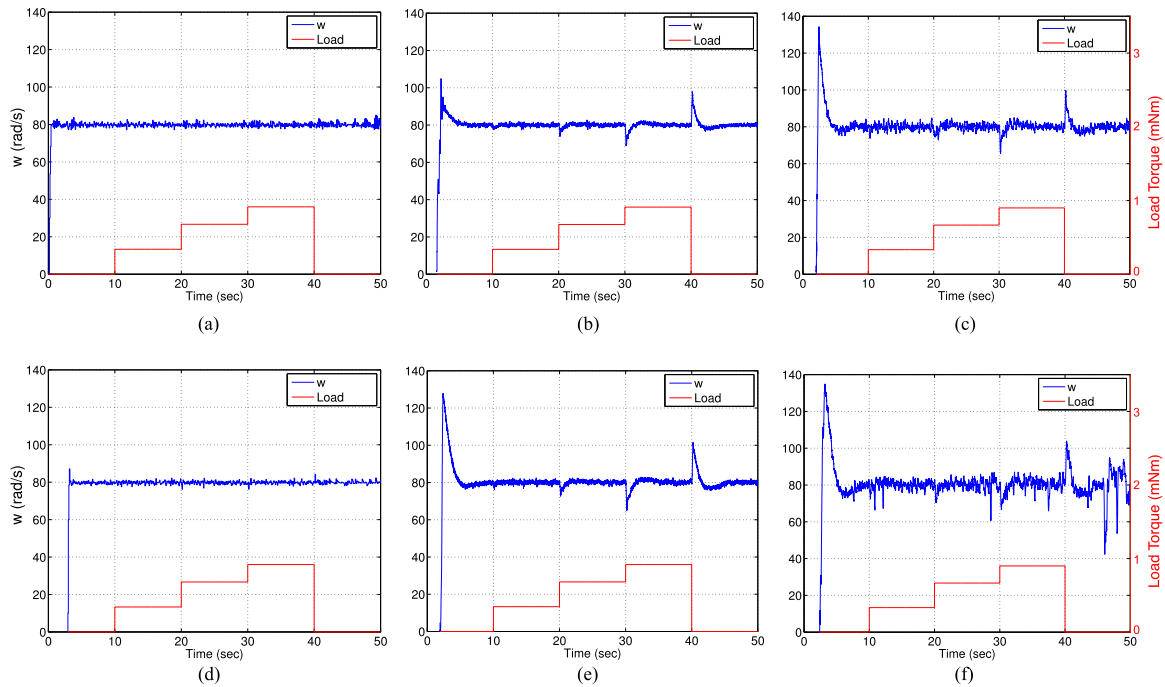


Fig. 8. Load disturbance rejection response for SSC, FOC-Int, and FOC-Ext schemes at $h = 30$ mm and $h = 50$ mm. (a) SSC @ $h = 30$ mm. (b) FOC-Int. @ $h = 30$ mm. (c) FOC-Ext. @ $h = 30$ mm. (d) SSC @ $h = 50$ mm. (e) FOC-Int. @ $h = 50$ mm. (f) FOC-Ext. @ $h = 50$ mm.

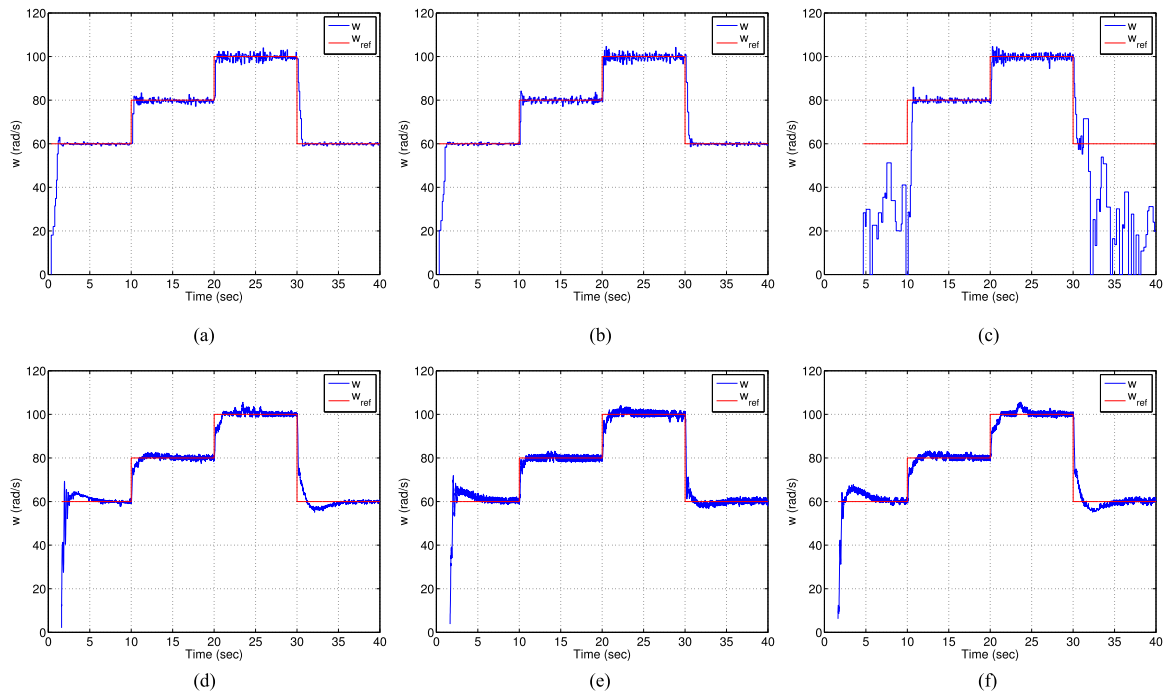


Fig. 9. Robustness of the speed tracking control schemes to axis misalignment in two cases: the PM rotor was shifted along the rotor shaft (X_{misalign}) and perpendicular to the shaft (Y_{misalign}) at $h = 30$ mm. (a) SSC @ ($X_{\text{misalign}} = 20$ mm, $Y_{\text{misalign}} = 0$). (b) SSC @ ($X_{\text{misalign}} = 0$, $Y_{\text{misalign}} = 20$ mm). (c) SSC @ ($X_{\text{misalign}} = 0$, $Y_{\text{misalign}} = 40$ mm). (d) FOC-Int. @ ($X_{\text{misalign}} = 20$ mm, $Y_{\text{misalign}} = 0$). (e) FOC-Int. @ ($X_{\text{misalign}} = 0$, $Y_{\text{misalign}} = 20$ mm). (f) FOC-Int. @ ($X_{\text{misalign}} = 0$, $Y_{\text{misalign}} = 40$ mm).

and FOC-Int control schemes. Stable performance is likely to be a result of relatively uniform field strength over a large volume under the windings, which is being generated due to large diameter of the windings (30 - mm diameter of metal core). However, as the misalignment was increased beyond 20 mm,

desynchronization was observed with SSC at low speeds. At the same time, FOC-Int was found to provide slower step response and higher overshoots. This was mainly due to the reduced maximum transmittable torque, proportional to the magnetic field strength, which decreases over distance. The FOC-Ext was

found to be capable only of rotating the rotor with 10-mm misalignment along the shaft ($X_{\text{misalign}} = 10 \text{ mm}$).

In reality, axis misalignments can be minimized through an appropriate anchoring unit. The anchoring unit, composed of an internal and an external PM, supports the weight of the internal instrument and the vertical forces applied during surgery. When placed correctly, the external and internal magnets will attract each other accurately by localizing their relative displacement to each other. Additionally, after instrument insertion into the abdominal cavity, a linear Hall effect sensor can be mounted in between the external anchoring electromagnet and abdominal wall surface to determine the location of internal anchoring PM by finding the location of strongest field. This would help to minimize misalignment.

VII. DISCUSSION AND CONCLUSION

The SCC has the advantages of simplicity in its algorithm, sensorless characteristics, and providing the fastest step response. Its main disadvantage is its predefined acceleration rate. Experiments have shown that an inappropriate selection of the acceleration rate may result in pole slipping and stall under lower external loads than those found in other control schemes. This problem becomes more evident when abdominal wall thickness increases or when misalignment is introduced, reducing the maximum transmittable torque. Another drawback is the inability to detect stall and regain synchronization with the rotor if it happens. An externally mounted Hall effect sensor could be used to improve this control scheme by restarting the controller to regain synchronization upon stall.

The speed response of the FOC was found to be slower than that of SSC, but it provides better steady-state performance, especially at higher speeds (see Table II). It also maintains synchronization during transients. The response of the controller to load disturbances revealed that it takes more time for the output speed to settle after disturbance. This is due to the fact that vector control adjust torque while maintaining a constant 90° angle between the rotor and the rotating field axes, which takes time. This is in contrast to SSC, which provides the maximum field strength at all time, which results in a very fast response to load disturbances.

Another advantage of the FOC is its capability to provide higher maximum transmittable torque. It has been demonstrated that due to its ability to maintain synchronization, this control scheme can transmit considerably higher torque before stalling (1.5 mN·m with FOC versus 1 mN·m with SSC). These are nongear figures, where appropriate gear ratio has been used to achieve much higher torque [8]. The FOC requires the feedback of angular position of the rotor. The internal Hall effect sensor used in the experiment was found to be effective in this respect, which introduces the need for a sensor on-board the internal device. However, this may not be a big issue from clinical standpoint as surgeons prefer to have a tether to retrieve the instrument if something is amiss.

The FOC with an externally mounted Hall effect sensor, which provides the advantage of a sensorless internal device, resulted in sufficiently accurate performance for the FOC when abdominal wall thickness $h = 30 \text{ mm}$. However, the investiga-

TABLE III
OFF-THE-SHELF COMMERCIAL DC MOTORS [7] COMPARABLE WITH THE SIZE OF THE PM ROTOR IN THE LEMA AT DIFFERENT ABDOMINAL WALL THICKNESS

Model	Diameter	Length	Max speed	Stall torque
LEMA@h = 23 mm	9.5 mm	9.5 mm	2850 r/min	3.1 mN·m
LEMA@h = 33 mm	9.5 mm	9.5 mm	2850 r/min	1.5 mN·m
LEMA@h = 43 mm	9.5 mm	9.5 mm	2850 r/min	1.1 mN·m
Namiki-SBL04	4 mm	13.8 mm	7000 r/min	0.13 mN·m
Faulhaber-1016	10 mm	16mm	18 400 r/min	0.87 mN·m
Faulhaber-1024	10 mm	24 mm	14 700 r/min	2.89 mN·m
Maxon-DCX10L	10 mm	25 mm	12 000 r/min	5.42 mN·m
Faulhaber-1224	12 mm	24 mm	13 800 r/min	3.62 mN·m
Precision-NC110	12 mm	12.5 mm	10 000 r/min	0.50 mN·m
Precision-MC112	12 mm	20 mm	9500 r/min	1.50 mN·m
Namiki-SCL12	12.5 mm	32 mm	13 750 r/min	3.71 mN·m

tion also found that angular position errors become too large for the FOC to function reliably when distance h is increased or misalignment is introduced. Further studies would be required to improve the practicality of this approach.

Comparison to the PM version of LMA [7] shows similar steady-state speed tracking error and maximum torque in general. The advantage of the LEMA was observed in the lower ripple in the speed tracking with load disturbance due to the use of two variable magnetic fields instead of one in the PM based. Additionally, the FOC approach in the LEMA maintains synchronization in a wider range of operating conditions, including axis misalignments up to 2 cm and in large loads exceeding maximum torque of 1 mN·m.

Table III compares the torque and the speed of the LEMA with off-the-shelf dc motors that have a diameter comparable with the PM rotor used in the LEMA. The maximum current rating of 5 A and the input voltage of 6 V in the current LEMA setup results in a maximum speed of 300 rad/s (2850 r/min). The stall torque in the LEMA is 1.1–3.1 mN·m depending on the abdominal wall thickness. Considering the size of the PM rotor 9.5 mm in both diameter and length, the LEMA can provide a volumetric power density that is well above any of the dc motors listed in Table III. For instance, the current LEMA setup at distance $h = 30 \text{ mm}$ delivers a nominal torque of approximately 1 mN·m using the SSC method (speed/torque gradient of 2850 r/min/mN·m). This is comparable in performance to a dc micromotor Maxon DCX10L, which provides 2.2-mN·m nominal torque (speed/torque gradient: 2240 r/min/mN·m), with diameter and length of 10 and 25 mm, respectively. Compared to dc motors, the emerging LEMA option is yet to be further optimized and carries the major advantage of having its stator coils external to the abdominal cavity and, thus, can be conveniently scaled to a larger capacity.

The LEMA approach was designed primarily for surgical manipulation tasks in the abdominal cavity. The abdominal cavity was chosen as it provided sufficient space for the manipulator to be inserted completely and to be exploited for its ability to cover the various quadrants in the abdominal space.

At this point, the authors are aiming toward a first test, i.e., the cholecystectomy procedure (gall bladder removal), where

TABLE IV
APPROXIMATE FORCE AND SPEED REQUIRED IN VARIOUS SURGICAL TASKS

Surgical tasks	Force	Speed	Ref
Liver and gall bladder retraction	6.6 N	N/A	[23]
Surgical camera	0.2 N	18 °/s	[6]
Surgical manipulation (e.g., pushing)	5 N	< 360 °/s	[6]
Soft tissue (e.g., liver penetration)	0.08 N	1 mm/s	[24]
Soft tissue (e.g., liver resection)	0.9 N	3 mm/s	[25]
Suturing (on soft tissue, e.g., skin)	1.7 N	5 mm/s	[26]
Suturing (pulling and tying knot)	8 N	N/A	[26]

the manipulator is required to first perform liver retraction and, then, to grasp and gently pull on the gall bladder to keep it taut for the incision to be made with a second surgical tool. The torque produced directly by the LEMA rotor (the 3 mN·m at a close distance), and its resulting speed (i.e., torque speed performance) is traded off using a selected gearhead to the appropriate torque speed operating condition required. A choice of miniaturized planetary gearhead of Broadway Gear Ltd. with a ratio of 1:200 brings our output torque to 0.6 N·m. In a liver retraction task, for example, the maximum reach of the required manipulator within the insufflated abdominal cavity is 10 cm (or 0.1 m). Thus, the lifting force it is capable of is around $0.6 \text{ N}\cdot\text{m}/0.1 \text{ m} = 6 \text{ N}$, which is in the ball park figure of the forces required for the liver and gall bladder retraction task, as listed in Table IV. Various design parameters can still be optimized.

The task of liver retraction was identified as requiring four DOFs. That makes eight coils (four pairs), which according to our current prototype, could all fit on one half of the external surface of an insufflated abdomen. That still makes a reasonably feasible or practical solution, which still has plenty of room for improvement.

In the future work, modeling and control of the multi-DOF LEMA system will be investigated. The effect of the actuation magnetic field produced by a set of stators may be felt at the neighboring rotors, resulting in disturbance. Such an effect will be first investigated to quantify the extend of its magnitude, and effective control strategies will then be designed. The viscoelastic nature of the abdominal wall would also be considered in the equation of motion of the LEMA system.

REFERENCES

- [1] A. G. Harrell and B. T. Heniford, "Minimally invasive abdominal surgery: Lux et veritas past, present, and future," *Amer. J. Surg.*, vol. 190, no. 2, pp. 239–243, 2005.
- [2] M. A. Carbajo *et al.*, "Laparoscopic treatment vs open surgery in the solution of major incisional and abdominal wall hernias with mesh," *Surgical Endoscopy*, vol. 13, no. 3, pp. 250–252, 1999.
- [3] A. N. Fader and P. F. Escobar, "Laparoendoscopic single-site surgery (LESS) in gynecologic oncology: Technique and initial report," *Gynecol. Oncol.*, vol. 144, no. 2, pp. 157–161, 2009.
- [4] G. Tortora, M. Salerno, T. Ranzani, S. Tognarelli, P. Dario, and A. Menciasci, "A modular magnetic platform for natural orifice transluminal endoscopic surgery," in *Proc. 35th Annu. Int. Conf. IEEE Eng. Med. Biol. Soc.*, 2013, pp. 6265–6268.
- [5] M. Piccigallo *et al.*, "Design of a novel bimanual robotic system for single-port laparoscopy," *IEEE/ASME Trans. Mechatronics*, vol. 15, no. 6, pp. 871–878, Dec. 2010.
- [6] F. Leong *et al.*, "Magnetic surgical instruments for robotic abdominal surgery," *IEEE Rev. Biomed. Eng.*, vol. 9, pp. 66–78, 2016.
- [7] C. Di Natali, J. Buzzi, N. Garbin, M. Beccani, and P. Valdastrì, "Closed-loop control of local magnetic actuation for robotic surgical instruments," *IEEE Trans. Robot.*, vol. 31, no. 1, pp. 143–156, Feb. 2015.
- [8] N. Garbin, C. Di Natali, J. Buzzi, E. De Momi, and P. Valdastrì, "Laparoscopic tissue retractor based on local magnetic actuation," *J. Med. Devices*, vol. 9, no. 1, 2015, Art. no. 011005.
- [9] MAGEC, Ellipse Technologies, 2016. [Online]. Available: <http://www.ellipse-tech.com/>
- [10] R. Montague, C. Bingham, and K. Atallah, "Servo control of magnetic gears," *IEEE/ASME Trans. Mechatronics*, vol. 17, no. 2, pp. 269–278, Apr. 2012.
- [11] A. Mohammadi, C. Di Natali, D. Samsonas, P. Valdastrì, Y. Tan, and D. Oetomo, "Electromagnetic actuator across abdominal wall for minimally invasive robotic surgery," *ASME J. Med. Devices*, vol. 9, no. 3, 2014, Art. no. 030937.
- [12] A. Mohammadi, D. Samsonas, C. Di Natali, P. Valdastrì, Y. Tan, and D. Oetomo, "Speed control of non-collocated stator-rotor synchronous motor with application in robotic surgery," in *Proc. 10th Asian Control Conf.*, 2015, pp. 1–6.
- [13] X. Zhang, L. Sun, K. Zhao, and L. Sun, "Nonlinear speed control for PMSM system using sliding-mode control and disturbance compensation techniques," *IEEE Trans. Power Electron.*, vol. 28, no. 3, pp. 1358–1365, Mar. 2013.
- [14] K. Kubota and K. Matsuse, "Speed sensorless field-oriented control of induction motor with rotor resistance adaptation," *IEEE Trans. Ind. Appl.*, vol. 30, no. 5, pp. 1219–1224, Sep./Oct. 1994.
- [15] M. P. Milad and M. F. Terkildsen, "The spinal needle test effectively measures abdominal wall thickness before cannula placement at laparoscopy," *J. Amer. Assoc. Gynecol. Laparoscopists.*, vol. 9, no. 4, pp. 514–518, 2002.
- [16] E. P. Furlani, *Permanent Magnet and Electromechanical Devices: Materials, Analysis, and Applications*. New York, NY, USA: Academic, 2001.
- [17] J. I. Itoh, N. Nomura, and H. Ohsawa, "A comparison between V/f control and position-sensorless vector control for the permanent magnet synchronous motor," in *Proc. IEEE Power Convers. Conf.*, 2002, vol. 3, pp. 1310–1315.
- [18] G. Kohlrusz and D. Fodor, "Comparison of scalar and vector control strategies of induction motors," *Hungarian J. Ind. Chem.*, vol. 39, no. 2, pp. 265–270, 2011.
- [19] J. R. B. Monteiro, A. A. Oliveira, M. L. D. Aguiar, and E. R. Sanagiotti, "Electromagnetic torque ripple and copper losses reduction in permanent magnet synchronous machines," *Int. Trans. Elect. Energy Syst.*, vol. 22, no. 5, pp. 627–644, 2012.
- [20] R. Kelly, J. Llamas, and R. Campa, "A measurement procedure for viscous and coulomb friction," *IEEE Trans. Instrum. Meas.*, vol. 49, no. 4, pp. 857–861, Aug. 2000.
- [21] C. Di Natali, A. Mohammadi, D. Oetomo, and P. Valdastrì, "Surgical robotic manipulator based on local magnetic actuation," *J. Med. Devices*, vol. 9, no. 3, 2015, Art. no. 030936.
- [22] F. Leong, A. Mohammadi, Y. Tan, P. Valdastrì, and D. Oetomo, "Experimentally validated modelling of electromechanical dynamics on local magnetic actuation system for abdominal surgery," in *Proc. Australas. Conf. Robot. Autom.*, 2016.
- [23] M. Cadeddu, M. Boyd, and P. Swain, "Retraction force measurement during transgastric and transvaginal notes," *Gastrointestinal Endoscopy*, vol. 67, no. 5, p. AB119, 2008.
- [24] F. Leong, W. H. Huang, and C. K. Chui, "Modeling and analysis of coagulated liver tissue and its interaction with a scalpel blade," *Med. Biol. Eng. Comput.*, vol. 51, no. 6, pp. 687–695, 2013.
- [25] A. M. Okamura, C. Simone, and M. D. O'Leary, "Force modeling for needle insertion into soft tissue," *IEEE Trans. Biomed. Eng.*, vol. 51, no. 10, pp. 1707–1716, Oct. 2004.
- [26] T. B. Frick, D. D. Marucci, J. A. Cartmill, C. J. Martin, and W. R. Walsh, "Resistance forces acting on suture needles," *J. Biomechanics*, vol. 34, no. 10, pp. 1335–1340, 2001.



Alireza Mohammadi received the B.Sc. degree in mechanical engineering from the Iran University of Science and Technology, Tehran, Iran, in 2005; the M.Sc. degree in mechanical engineering from the Sharif University of Technology, Tehran, in 2008; and the Ph.D. degree from the University of Melbourne, Parkville, VIC, Australia, in 2014.

He is currently a Postdoctoral Research Fellow with the University of Melbourne. His research interests include applied control theory

and medical robotics.



Dhan Thiruchelvam received the Bachelor of Medicine/Bachelor of Surgery (M.B.B.S.) degree in medicine and surgery from the University of Sydney, Sydney, NSW, Australia, in 1999 and the diploma in clinical education from the University of Edinburgh, Edinburgh, U.K., in 2011.

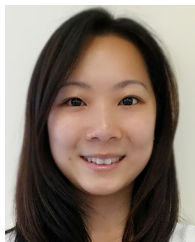
He is an Upper GI and Obesity Surgeon with St. Vincent's Hospital, Fitzroy, VIC, Australia. His research interests include robotic surgery and surgical education.

Dr. Thiruchelvam is a fellow of the Royal Australasian College of Surgeons.



Danielius Samsonas received the Bachelor of Physics degree in modern technologies and management from Vilniaus Universitetas, Vilnius, Lithuania, in 2012, and the M.Eng. degree in mechanical engineering from the University of Nottingham, Nottingham, U.K., in 2016.

He is currently with the University of Melbourne, Parkville, VIC, Australia. His research interests include surgical robotics.



Florence Leong received the M.Eng. degree in medical robotics/biomechanics from the National University of Singapore, Singapore, in 2010. She is currently working toward the Ph.D. degree in medical robotics with the University of Melbourne, Parkville, VIC, Australia.

Her current research interests include the development of a transabdominal local electromagnetic actuator for abdominal surgery.



Ying Tan received the B.E. degree in electrical engineering from Tianjin University, Tianjin, China, in 1995, and the Ph.D. degree in electrical engineering from the National University of Singapore, Singapore, in 2002.

She was a Research Fellow with McMaster University, ON, Canada. In 2004, she joined the University of Melbourne, Parkville, VIC, Australia, where she is currently an Associate Professor and Reader. Her research interests include intelligent systems, nonlinear control systems,

real-time optimization, and sampled-data distributed parameter systems.



Pietro Valdastrì (M'05–SM'13) received the master's (hons.) degree in electronic engineering from the University of Pisa, Pisa, Italy, in 2002, and the Ph.D. degree in biomedical engineering from the Sant'Anna School of Advanced Studies, Pisa, in 2006.

He is a Professor and Chair in robotics and autonomous systems with the University of Leeds, Leeds, U.K. His research interests include robotic surgery, design of magnetic mechanisms, and medical capsule robots.

Dr. Valdastrì received the Wolfson Research Merit Award from the Royal Society.



Denny Oetomo (M'04–SM'11) received the B.Eng. (hons.) degree in mechanical engineering from Australian National University, Canberra, ACT, Australia, in 1997, and the Ph.D. degree from the National University of Singapore, Singapore, in 2004.

His research interests include robotic manipulation with applications mainly in the areas of clinical/biomedical engineering. He was a Research Fellow at Institut National de Recherche en Informatique et en Automatique (INRIA) in

Sophia-Antipolis in 2007. In 2008, he joined the University of Melbourne, Parkville, VIC, Australia, where he is currently an Associate Professor.